The Thesis Committee for Bryant Minh Tran
Certifies that this is the approved version of the following thesis:

Three Transdimensional Factors for the Conversion of 2D Acoustic Rough Surface Scattering Model Results for Comparison with 3D Scattering

APPROVED BY

SUPERVISING COMMITTEE:

Preston Wilson, Supervisor

Marcia Isakson, Co-Supervisor

Three Transdimensional Factors for the Conversion of 2D Acoustic Rough Surface Scattering Model Results for Comparison with 3D Scattering

by

Bryant Minh Tran, B.S.E.E.

THESIS

Presented to the Faculty of the Graduate School of
The University of Texas at Austin
in Partial Fulfillment
of the Requirements
for the Degree of

MASTER OF SCIENCE IN ENGINEERING

THE UNIVERSITY OF TEXAS AT AUSTIN
December 2013

Acknowledgments

I'd like to acknowledge the tireless support of everyone who helped me through my Masters program. Eric Hatcher, the first person to fund me and offer me the opportunity to develop my MATLAB skills, Dr. Preston Wilson for showing me the world of acoustics and advising me throughout my time studying it, Dr. Mark Hamilton for teaching me almost everything I know about physical acoustics and scientific thought, my parents Binh and Kim Khanh Tran and sister Kristen Tran for putting up with me going to school for another three and a half years, and finally Dr. Marcia Isakson for supervising me, showing me the art of COMSOL and rough surface scattering, teaching me underwater acoustics, and providing me with a path to graduation.

Furthermore, I'd like to acknowledge the support of ONR Ocean Acoustics, who supported this work, and the Texas Advanced Computing Center (TACC) at The University of Texas at Austin for providing HPC resources that have contributed to the research results reported within this thesis.

I'd also like to thank the numerous students and coworkers who, without their help, I would have had a lonely, lonely existence. Special thanks to my office mates Anthony Bonomo and Benjamin Goldsberry for showing me how to shoot a basketball. And lastly to Dr. Adam Metzler, my mentor whether he liked it or not.

Three Transdimensional Factors for the Conversion of 2D Acoustic Rough Surface Scattering Model Results for Comparison with 3D Scattering

Bryant Minh Tran, M.S.E.
The University of Texas at Austin, 2013

Supervisors: Preston Wilson
Marcia Isakson

Rough surface scattering is a problem of interest in underwater acoustic remote sensing applications. To model this problem, a fully three-dimensional (3D) finite element model has been developed, but it requires an abundance of time and computational resources. Two-dimensional (2D) models that are much easier to compute are often employed though they don't natively represent the physical environment. Three quantities have been developed that, when applied, allow 2D rough surface scattering models to be used to predict 3D scattering. The first factor, referred to as the spreading factor, adopted from the work of Sumedh Joshi [1], accounts for geometrical differences between equivalent 2D and 3D model environments. A second factor, referred to as the perturbative factor, is developed through the use of small perturbation theory. This factor is well-suited to account for differences in the scattered field between a 2D model and scattering from an isotropically rough 2D surface in 3D. Lastly, a third composite factor, referred to as the combined factor, of the previous two is developed by taking their minimum. This work deals only with scattering within the plane of the incident wave perpendicular to the scatterer. The applicability of these factors are tested by comparing a 2D scattering model with a fully three-dimensional Monte Carlo finite element method model for a variety of von Karman and Gaussian power spectra. The combined factor shows promise towards a robust method to adequately characterize isotropic 3D rough surfaces using 2D numerical simulations.

Table of Contents

List of Tables

List of Figures

Chapter 1

Introduction

Acoustic scattering from rough surfaces is a problem of much interest and research in the shallow-water acoustics community due to the interaction of sound waves with both the seafloor and the sea surface. Many different acoustical remote sensing apparatuses such as side-scan sonar, synthetic aperture sonar, and echo-sounding fathometers rely on these reflections to operate [3]. For these applications, roughness adds complexity and uncertainty to appropriately interpreting sonar returns. Furthermore, in long-range applications such as in the case of passive sonar surveillance, roughness introduces additional transmission loss and reverberation noise that result in altered propagation loss and miscalculated detection probabilities that can be devastating to sonar effectiveness.

This work deals with the effects of roughness in mainly active sonar applications. Unlike other underwater acoustics problems (e.g. long-range transmission loss), large bathymetric features are ignored in favor of features of a size on the order of the wavelength of interest. Due to exploration of this topic in fields such as radar and digital communications, much of this work makes use of similar mathematics and vocabulary found in the electromagnetism community.

Approximate scattering models have been developed going back to Lord Rayleigh's *Theory of Sound*, which presented a predecessor to modern small perturbation theory for sinusoidally rough surfaces [4]. This was expanded in the electromagnetics community through the work of Fano [5] and, later, Rice [6]. These formulations have been tested numerically for acoustic waves scattering off 1D rough surfaces characterized by a Gaussian power spectrum. The finite element method for this application has been used in recent years through the work of Isakson [7, 8]. In 2001, a topical survey concluded that efficient 3D rough surface scattering models were needed [9]. Joshi developed a fully three-dimensional finite element model for scattering from rough pressure-release surfaces and developed a "correction" to compare 2D and 3D results, referred to, in this work, as the "spreading factor" [1].

The primary purpose of this work is to explore the differences between scattering of different dimensions. Two-dimensional numerical models are easier to compute, but they inherently represent an unrealistic physical system whereas three-dimensional models better approximate realistic environments but require an order of magnitude increase in computational complexity. A previous study has shown that although a 3D finite element model may take close to 30 minutes to compute, a 2D finite element model takes only a minute to solve while requiring less of the computer's random access memory (RAM) [1].

In order to remedy the unrealistic nature of 2D models while preserving their computational advantage, easily computed conversion factors are developed to quantify the differences between the two-dimensional and three-dimensional rough surface scattering. The document is organized as follows: In Chapter 2, the statistics that govern the characterization of rough surfaces are discussed. Then the model environment is described in Chapter 3. Perturbation theory is then derived and the finite element method is explained in Chapters 4 and 5, respectively. In Chapter 6, the spreading, perturbative, and combined transdimensional factors are derived. They are applied to six different parameter sets in Chapter 7. And finally conclusions and possibilities for future work are provided in Chapter 8.

It is shown that both the spreading and perturbative factors provide insight into the conversion of coherent and incoherent scattered energy from two-dimensional to three-dimensional environments, respectively, for von Karman surfaces. The effectiveness of the spreading factor, derived from the comparison of flat surfaces, near the specular peak shows that the coherent scattered field behaves similarly to that of a flat surface, and the perturbative factor, effectively a ratio of power spectra, suggests that the change in the incoherent field between two and three dimensions can be approximated by the change in roughness. The use of these factors in conjunction with 2D model results provides a usable method for comparison to 3D scattering.

Chapter 2

Rough Surface Statistics

Rough surfaces are prevalent in the ocean. They arise from a number of sources including unsteady flow of the seawater, turbulence, fish, wind, and varying particle sizes of the seafloor. These contributions add a variety of scales of roughness. It is important to distinguish between roughness that causes acoustic scattering and larger features, which contribute to the slope of the floor. The roughness that is discussed in this thesis refers to the variations in the seafloor or surface that contribute to incoherent scattering. Specifically, roughness on this scale cannot steer the coherent field in a new direction. Mathematically, this corresponds to roughness on the order of a wavelength and smaller [3].

The roughness is characterized by its deviation from the mean or smooth surface. This is known as the surface relief function (SRF). The SRF itself represents deviation in the third spatial dimension (z). In three dimensions, the SRF is a function of two variables, the cross dimensions (x, y). In two dimensions, the SRF is a function of only one variable (x). The SRF is also zero-mean.

2.1 Random Rough Surfaces

For modeling, the surface relief function is assumed to be a random variable characterized by a power spectrum, defined as

$$W(\mathbf{K}) = \frac{\sigma^2}{(2\pi)^2} \int_{-\infty}^{\infty} C(\mathbf{R}) e^{i\mathbf{k}\cdot\mathbf{R}} d\mathbf{R}, \tag{2.1}$$

where σ^2 is the variance of the surface, $C(\mathbf{R})$ is the correlation function, $\mathbf{K}$ is the wavevector, and $\mathbf{R}$ is the spatial vector. To calculate the power spectrum for a measured section of the ocean floor, the following two simplified formulas that assume wide-sense stationarity are used:

$$W_1(K_x) = \frac{1}{2\pi L} |F_1(K_x)|^2 \tag{2.2}$$

and

$$W_2(K_x, K_y) = \frac{1}{(2\pi L)^2} |F_2(K_x, K_y)|^2, \tag{2.3}$$

where $F_1(K_x)$ denotes the 1D Fourier transform of the 1D surface relief function and $F_2(K_x, K_y)$ denotes the 2D Fourier transform of the 2D surface relief function.

It has been shown that the power spectra of the sea floor conform well to the von Karman spectrum given by [3]

$$W_{2,\mathrm{VK}}(K) = \frac{w_2}{(K^2 + K_L^2)^{\gamma_2/2}}, \tag{2.4}$$

for 2D surfaces and

$$W_{1,\mathrm{VK}}(K) = \frac{w_1}{(K^2 + K_L^2)^{\gamma_1/2}}, \tag{2.5}$$

for 1D surfaces, where w is the spectral strength, γ is the spectral exponent, K_L is the cutoff wavenumber, and K is the magnitude of the spatial wavevector. The subscript VK refers to 'von Karman.' This form comes from the turbulence community [10]. It is often substituted by the simplified power-law spectrum

$$W(K) = \frac{w}{K^{\gamma}}. \tag{2.6}$$

Another form used for roughness statistics is the Gaussian roughness spectrum though it doesn't match measured results as closely as the von Karman spectrum. This is given by

$$W_{1,\mathrm{G}}(K) = \frac{lh^2}{\sqrt{4\pi}} e^{-K^2 l^2/4} \tag{2.7}$$

for 1D and

$$W_{2,\mathrm{G}}(K) = \frac{l^2 h^2}{4\pi} e^{-K^2 l^2/4} \tag{2.8}$$

for 2D, where l refers to the correlation length, h is root-mean-square (RMS) height, and K is the magnitude of the wavevector. The subscript G refers to 'Gaussian.'

In order to employ Monte Carlo methods, realizations of the rough surface are generated using a Gaussian height distribution and uniformly randomized phase. Computationally, this is accomplished using Eq. (2.9) [11].

$$\zeta(x) = \mathcal{F}^{-1}\left\{\sqrt{2\pi L W_1(K)} \times \frac{N(0,1) + iN(0,1)}{\sqrt{2}}\right\}, \tag{2.9}$$

where $N(0,1)$ refers to a normal distribution with zero mean and unit standard deviation, $\mathcal{F}^{-1}$ is the inverse Fourier transform. Equivalently for 2D surfaces, this is accomplished using Eq. (2.10).

$$\zeta(x) = \mathcal{F}^{-1}\left\{\sqrt{(2\pi L)^2 W_2(K)} \times \frac{N(0,1) + iN(0,1)}{\sqrt{2}}\right\}, \tag{2.10}$$

Equations (2.9) and (2.10) are both implemented discretely using the inverse fast Fourier transform (IFFT).

2.2 Transdimensional Roughness Statistics

Surface reliefs are generally measured along a single direction. In order to calculate models that use 2D roughness statistics from these measurements, either longitudinal invariance (LI) or isotropy is assumed. Longitudinal invariance can be implemented simply by asserting that the surface relief function does not vary in y, the longitudinal direction.

$$\zeta(x, y) = \zeta(x) \tag{2.11}$$

On the other hand, isotropic roughness is implemented by asserting that the roughness power spectrum only depends on the magnitude of the wavevector.

$$W_2(K_x, K_y) = W(K, \phi) = W(K), \tag{2.12}$$

where $K = \sqrt{K_x^2 + K_y^2}$ is the magnitude of the wavevector and ϕ is its angle. In order to preserve RMS height and roughness statistics along a 1D transect, the Abel transform is used [3].

$$W_2(K) = \frac{1}{\pi}\int_0^\infty \frac{W_1(K) - W_1(\sqrt{K^2 + q^2})}{q^2} dq \tag{2.13}$$

For the von Karman spectrum, if the 1D power spectrum is defined as

$$W_1(K) = \frac{w_1}{(K^2 + K_L^2)^{\gamma_1/2}}, \tag{2.14}$$

then

$$W_2(K) = \frac{w_2}{(K^2 + K_L^2)^{\gamma_2/2}}, \tag{2.15}$$

where

$$w_2 = w_1 \frac{\Gamma(\frac{\gamma_2}{2})}{\sqrt{\pi}\Gamma(\frac{\gamma_2 - 1}{2})} \tag{2.16}$$

$$\gamma_2 = \gamma_1 + 1 \tag{2.17}$$

For the Gaussian spectrum, no conversion of the RMS height h or the correlation length l is needed.

Chapter 3

Model Environment

In this thesis, a simplified form of the physical problem is employed to isolate scattering from other factors that affect acoustic propagation underwater. While in reality, the environment most affected by seafloor scattering is the shallow water waveguide, which involves multiple reflections from both the sea surface and seafloor, this work makes use of an idealized model that contains a single reflection from only the seafloor. Furthermore, the scattering surface is modeled as a Dirichlet boundary condition, specifically the pressure-release condition ($p = 0$). This has been used in the past in a thesis [1] as well as in papers and books [3, 2, 11, 12, 13, 14] . It allows for solving the problem in a water-filled infinite half-space above the rough boundary. The water is assumed to be homogeneous and still with a sound speed of 1529 m/s and a density of 1026 kg/m^3, values consistent with seawater [7].

The simplest setup involves an incident plane wave with wavevector in the $x - z$ plane incident on the rough surface and scattering into any number of directions with wave vector $\mathbf{k}_s$. Figure 3.1 shows the angle convention used in this work: θ_g is the grazing angle, measured between the incident wave vector and the negative x direction, θ_s is the scattered angle, measured between the scattered wave vector and the mean plane of the rough surface, and ϕ_s is the angle counterclockwise from the positive x direction of the scattered wave vector projected onto the $x - y$ plane. This work only considers scattering with wavevectors also in the $x - z$ plane ($\phi_s = 0$). To simplify the convention for this case, θ_s is redefined to be the angle between the scattered wave vector and the positive x direction. For analytical models, a progressive plane wave is incident on the rough surface of the form

$$p_i = Ae^{i(\omega t - \mathbf{k}\cdot\mathbf{r})}, \tag{3.1}$$

where ω is the angular frequency of excitation, t is time, $\mathbf{k} = k\cos\theta_i\mathbf{e}_x - k\sin\theta_i\mathbf{e}_z$ is the incident wavevector, $k = \omega/c$ is the acoustic wavenumber, and $\mathbf{r} = x\mathbf{e}_x + y\mathbf{e}_y + z\mathbf{e}_z$ is the field point. Vector quantities are indicated using boldface and $\mathbf{e}_x$, $\mathbf{e}_y$, $\mathbf{e}_z$ are the unit vectors corresponding to the positive x, y, and z directions, respectively. A is chosen such that the wave has unit intensity. The equation for the incident field is then

$$p_i(\mathbf{r}, t) = \sqrt{\rho_0 c_0}e^{i(\omega t - \mathbf{k}\cdot\mathbf{r})}. \tag{3.2}$$

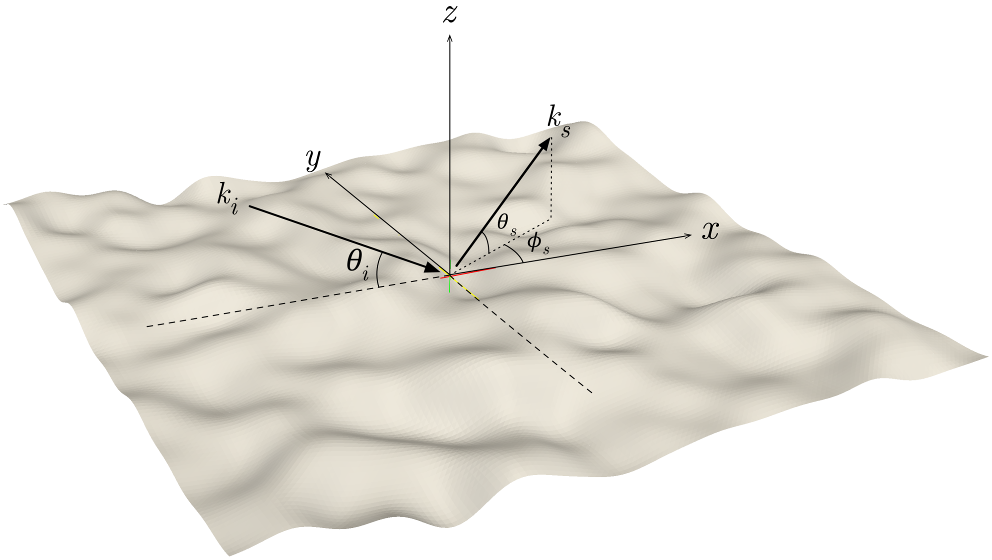

Figure 3.1: Incident (k_g) and scattered (k_s) wavevectors in three dimensions with angle convention. Rough surface shown modeled as pressure release. Results shown in this work show scattering where $\phi_s = 0$.

Chapter 4

Small-Roughness Perturbation Theory

Calculating roughness scattering using an approximate method is a well-established area of research [14]. One of the most widely used methods is small-roughness perturbation theory, sometimes referred to as small perturbation theory or simply perturbation theory. This solution describes a class of solutions that is valid for 'slightly rough' surfaces [12]. Its defining characteristic is the separation of the field into a number of perturbative orders around the unperturbed case, reflection from a flat surface.

If it is assumed that the surface is generally flat (i.e. $|k\nabla\zeta(\mathbf{r}_0)| \ll 1$), one can perform an expansion on both the scattered and incident pressure fields around the mean plane of the scattering surface as follows

$$p(\mathbf{r}_0,\zeta) = p(\mathbf{r}_0,0) + \zeta(\mathbf{r}_0)\left.\frac{\partial p(\mathbf{r}_0,z)}{\partial z}\right|_{z=0} + \zeta(\mathbf{r}_0)^2\left.\frac{\partial^2 p(\mathbf{r}_0,z)}{\partial z^2}\right|_{z=0} + \mathcal{O}(\zeta^3), \quad (4.1)$$

where $\zeta = \zeta(\mathbf{r}_0)$ is the "surface relief function," as is explained in section 2.1, $\mathbf{r}_0$ is a point on the mean plane of the rough surface, and p is acoustic pressure. If $k|\zeta| \ll 1$, it is sufficient to take the expansion only to first order.

A perturbation theory solution formulated for a pressure-release boundary condition can be represented as

$$p_i(\mathbf{r},\zeta) + p_s(\mathbf{r},\zeta) = 0, \quad (4.2)$$

where p_i is the pressure incident on the scatterer and p_s is the scattered pressure. Substituting Eq. (4.1) into Eq. (4.2), retaining only terms of $\mathcal{O}(\zeta)$, this can be rewritten as

$$p_i(\mathbf{r}_0, 0) + \zeta(\mathbf{r}_0)\, \frac{\partial p_i(\mathbf{r}_0, z)}{\partial z}\bigg|_{z=0} + p_s(\mathbf{r}_0, 0) + \zeta(\mathbf{r}_0)\, \frac{\partial p_s(\mathbf{r}_0, z)}{\partial z}\bigg|_{z=0} = 0. \tag{4.3}$$

Perturbation theory supposes that the scattered pressure can be written as

$$p_s = p_s^{(0)} + p_s^{(1)} + p_s^{(2)} + \cdots\,, \tag{4.4}$$

where $p_s^{(n)} = \mathcal{O}(\zeta^n)$. Substituting Eq. (4.4) into Eq. (4.3), retaining terms of $\mathcal{O}(\zeta)$ gives

$$p_i|_{z=0} + \zeta\, \frac{\partial p_i}{\partial z}\bigg|_{z=0} + p_s^{(0)}|_{z=0} + p_s^{(1)}|_{z=0} + \zeta\, \frac{\partial p_s^{(0)}}{\partial z}\bigg|_{z=0} = 0. \tag{4.5}$$

Equating terms of same order, the zeroth- and first-order boundary conditions are

$$p_i\big|_{z=0} + p_s^{(0)}\big|_{z=0} = 0 \tag{4.6}$$

$$\zeta\, \frac{\partial p_i}{\partial z}\bigg|_{z=0} + p_s^{(1)}\big|_{z=0} + \zeta\, \frac{\partial p_s^{(0)}}{\partial z}\bigg|_{z=0} = 0. \tag{4.7}$$

Equation (4.6) should be recognized as the boundary condition for reflection from a flat pressure-release boundary. This boundary condition can be applied to the Helmholtz-Kirchhoff integral.

$$p_s(\mathbf{r}) = \int_S \left[p(\mathbf{r}_0) \frac{\partial G(\mathbf{r}, \mathbf{r}_0)}{\partial \mathbf{n}_0} - G(\mathbf{r}, \mathbf{r}_0) \frac{\partial p(\mathbf{r})}{\partial \mathbf{n}_0} \right] \, \mathrm{d}S(\mathbf{r}_0), \tag{4.8}$$

where $p = p_i + p_s$ is the total pressure and G is an acoustic Green's function, $\mathbf{r}_0$ represents a point on the scattering surface, $\mathbf{n_0}$ is a unit normal vector to the surface, and S is the surface defined by the scatterer.

Applying Eq. (4.7) to Eq. (4.8) for just the first-order field gives

$$p_s^{(1)}(\mathbf{r}) = -\int_{S_M} \zeta(\mathbf{r}_0) \left(\frac{\partial p_i}{\partial z} + \frac{\partial p_s^{(0)}}{\partial z} \right) \frac{\partial G^*(\mathbf{r}, \mathbf{r}_0)}{\partial z_0} \, \mathrm{d}S_M(\mathbf{r}_0), \tag{4.9}$$

where S_M is the mean plane of the scatterer ($z = 0$) and $G^*(\mathbf{r}, \mathbf{r}_0)$ is the half-space Green's function where the asterisk signifies specialization of the Green's function to a half-space over a pressure-release boundary.

$$G^*_{\mathrm{3D}}(\mathbf{r}, \mathbf{r}_0) = \frac{e^{ik|\mathbf{r}-\mathbf{r}_0|}}{4\pi|\mathbf{r}-\mathbf{r}_0|} - \frac{e^{ik|\mathbf{r}-\mathbf{r}'_0|}}{4\pi|\mathbf{r}-\mathbf{r}'_0|}, \tag{4.10}$$

where $k = \omega/c$ is the natural wavenumber and if $\mathbf{r}_0 = (x, y, z)$, then $\mathbf{r}'_0 = (x, y, -z)$ in 3D. For 2D simulations, this Green's function is given by

$$G^*_{\mathrm{2D}}(\mathbf{r}, \mathbf{r}_0) = \frac{i}{4} H_0^{(1)}(k|\mathbf{r}-\mathbf{r}_0|) - \frac{i}{4} H_0^{(1)}(k|\mathbf{r}-\mathbf{r}'_0|), \tag{4.11}$$

where $H_0^{(1)}$ is a Hankel function of the first kind.

Now if it is assumed that the field point is sufficiently far away, the Green's function reduces to the following form for 3D:

$$G^*_{\mathrm{3D}}(\mathbf{r}, \mathbf{r}_0) = \frac{-ike^{ikr}}{2\pi r} \sin\theta_s e^{-i\mathbf{k_s}\cdot\mathbf{r}_0}, \tag{4.12}$$

where $r = |\mathbf{r}|$ is the receiver distance from the scatterer, and the wavevectors are described in Fig. 3.1 and are given by

$$k_i = k(\cos\theta_i \mathbf{e}_x - \sin\theta_i \mathbf{e}_z), \tag{4.13}$$

$$k_s = k(\cos\theta_s \cos\phi_s \mathbf{e}_x + \cos\theta_s \sin\phi_s \mathbf{e}_y + \sin\theta_s \mathbf{e}_z), \tag{4.14}$$

where $\mathbf{e}_x$, $\mathbf{e}_y$, $\mathbf{e}_z$ are the unit vectors corresponding to the positive x, y, and z directions, respectively. Asymptotically, as $|\mathbf{r}-\mathbf{r}_0| \to \infty$, the Hankel function is given by [15]

$$H_0^{(1)}(z) \sim \sqrt{\frac{2}{\pi z}} e^{-i\pi/4} e^{iz}. \tag{4.15}$$

By extension, the 2D far field Green's function is given by

$$G^*_{\mathrm{2D}}(\mathbf{r}, \mathbf{r}_0) = \sqrt{\frac{ik}{2\pi r}} e^{ikr} \sin\theta_s e^{-i\mathbf{k}_s \cdot \mathbf{r}_0}. \tag{4.16}$$

The far-field pressure can be converted to scattering cross section (per unit area) using the following formulas:

$$\sigma_{\mathrm{3D}} = \frac{\langle I_s \rangle r^2}{I_i A_M} \tag{4.17}$$

and

$$\sigma_{\mathrm{2D}} = \frac{\langle I_s \rangle r}{I_i L_M}, \tag{4.18}$$

where $\langle\rangle$ indicate ensemble average, I_s is the magnitude of scattered far-field intensity, r is the distance of the receiver from the surface, I_i is the magnitude of the incident intensity (prescribed to be unity in Chapter 3), A_M is the area of the mean plane in 3D, and L_M is the length of the surface mean in 2D [1, 11].

Ensemble averaged intensity is given by [16],

$$\langle I \rangle = \langle p\bar{p} \rangle / \rho_0 c_0, \tag{4.19}$$

where I is magnitude of intensity, p is complex pressure, $\bar{p}$ is the complex conjugate of complex pressure, ρ_0 is the equilibrium material density, and c_0 is the material sound speed. Recall that for the incident field, Eq. 3.2, intensity is unity ($I_i = \left(\sqrt{\rho_0 c_0}\right)^2 / \rho_0 c_0 = 1$). Substituting Eq. (4.9) into Eq. (4.19) leads to [12]

$$\begin{aligned}\langle I_s^{(1)}(\mathbf{r})\rangle = \sigma^2 \int\int C(\mathbf{r}_0 - \mathbf{r}_1) \left[\frac{\partial p_i(\mathbf{r}_0)}{\partial z} + \frac{\partial p_s^{(0)}(\mathbf{r}_0)}{\partial z}\right] \\ \times \left[\frac{\partial \bar{p}_i(\mathbf{r}_1)}{\partial z} + \frac{\partial \bar{p}_s^{(0)}(\mathbf{r}_1)}{\partial z}\right] \frac{\partial G^*(\mathbf{r}, \mathbf{r}_0)}{\partial z_0} \frac{\partial \bar{G}^*(\mathbf{r}, \mathbf{r}_0)}{\partial z_1} dS_{M0} dS_{M1}, \quad (4.20)\end{aligned}$$

where $C(\mathbf{r}_0 - \mathbf{r}_1) = \langle \zeta(\mathbf{r}_0))\zeta(\mathbf{r}_1)\rangle / \sigma^2$ is the correlation function of the SRF function assuming stationarity, σ^2 is the variance of the SRF, and $\mathbf{r}_0$ and $\mathbf{r}_1$ are points on the mean plane ($S_{M0} = S_{M1} = S_M$). Substituting Eqs. (4.16), (3.2) and (4.10) into Eq. 4.20 gives

$$\begin{aligned}\langle I_{s,3\mathrm{D}}^{(1)}(\mathbf{r})\rangle = \frac{k^4 \sigma^2 \sin^2\theta_g \sin^2\theta_s}{\pi^2 r^2} \\ \times \int\int C(\mathbf{r}_0 - \mathbf{r}_1) e^{ik[A(x_0 - x_1) + B(y_0 - y_1)]} dx_0 dy_0 dx_1 dy_1, \quad (4.21)\end{aligned}$$

where

$$A = \cos\theta_g - \cos\theta_s \cos\phi_s, \quad (4.22)$$

$$B = -\cos\theta_s \sin\phi_s \quad (4.23)$$

for 3D and

$$\langle I_{s,2\mathrm{D}}^{(1)}(\mathbf{r})\rangle = \frac{k^3 \sigma^2 \sin^2\theta_g \sin^2\theta_s}{\pi^2 r^2} \int\int C(\mathbf{r}_0 - \mathbf{r}_1) e^{ikA(x_0 - x_1)} dx_0 dx_1, \quad (4.24)$$

where

$$A = \cos\theta_g - \cos\theta_s \quad (4.25)$$

for 2D.

Recognizing the power spectrum (Equation (2.1)) in Eqs. (4.21) and (4.24) provide a much simpler form:

$$\langle I_{s,3\text{D}}^{(1)}(\mathbf{r})\rangle = \frac{k^4 \sin^2\theta_g \sin^2\theta_s}{r^2} A_M W_2(kA, kB), \tag{4.26}$$

where $W_2(K_x, K_y)$ is the 2D power spectrum and A_M is the area of the mean plane of the scattering surface, for 3D, and

$$\langle I_{s,3\text{D}}^{(1)}(\mathbf{r})\rangle = \frac{k^3 \sin^2\theta_g \sin^2\theta_s}{r^2} L_M W_1(kA), \tag{4.27}$$

where $W_1(K_x)$ is the 1D power spectrum and L_M is the length of the mean line of the scattering surface, for 2D.

Substituting into Eqs. (4.18) and (4.17) gives

$$\sigma_{\text{pt,3D}} = 4k^4 \sin(\theta_i)\sin(\theta_s) W_2(kA, kB) \tag{4.28}$$

and

$$\sigma_{\text{pt,2D}} = 4k^3 \sin(\theta_i)\sin(\theta_s) W_1(kA), \tag{4.29}$$

where the subscript pt refers to perturbation theory.

Since this work deals only with in-plane scattering ($\phi_s = 0$), $kB = 0$ and $kA = k(\cos\theta_g - \cos\theta_s)$, the difference between the horizontal wavenumbers of the incident and scattered wave.

This model is used in Section 6.2 to derive the perturbative factor in Chapter 6 and is also compared against the finite element method in Chapter 7.

Chapter 5

Finite Element Method

The finite element method (FEM), sometimes referred to as finite elements, is a computational technique used to solve ordinary and partial differential equations [17]. The commercial FEM package COMSOL Multiphysics 4.3b was used to perform the calculations for this work [18]. The steps to construct and solve a scattering FEM model will be described in five steps: geometry definition, mesh generation, parameter definition, solution, and boundary integration.

5.1 Geometry Definition

Perhaps the most user-intensive step to creating an FEM model using COMSOL is definition of the geometry. The purpose of this step is to define "domains" and "boundaries" that can be used to subdivide the computational domain. This structure is convenient especially for doing multiphysics applications, but it's also well-suited for setting up varied boundary conditions. This also allows for unattended mesh creation and simple boundary condition handling. Unfortunately, this step is difficult when dealing with random rough surfaces. In this work, a direct implementation of the roughness is prescribed in the geometry. There is another approach to adding roughness that was not used for this work, namely the “deformed geometry” interface (see Appendix A). For a 2D model (which predicts scattering off of a 1D rough surface), prescribing the roughness is simple to implement. Given the x and z coordinates of a random rough surface realization, a contour can be easily created, adequately defining the rough surface. This is in contrast to the more involved process of defining a 2D surface for 3D modeling. In that case, a set of x, y, and z coordinates are given on a uniform x-y grid to describe the surface height of the rough surface. Whereas connectivity is easily implied in the 2D simulation, connectivity is less obvious in the 3D case. For this work, diagonal connectivity is assigned arbitrarily, creating a triangular mesh that explicitly defines the rough surface.

The 3D geometry is shown in Fig. 5.1. This geometry was adopted from the work of Joshi [1]. A square rough surface patch was generated computationally in the software MATLAB using an FFT algorithm and the roughness outside of an inscribed circle was set to 0 and the surface height tapered to the edges. The patch sits in a cylindrical computational domain with attenuating layers constructed above and on the sides of this computational domain to approximate an infinite half-space condition. These layers are implemented using ‘perfectly matched layers,’ which are described in Sec. 5.3.

The 2D geometry is shown in Fig. 5.2. Whereas all boundaries in the 3D geometry met at right angles, the 2D geometry uses an alternate form that uses a circular exterior boundary. This is chosen to reduce the size of the com-

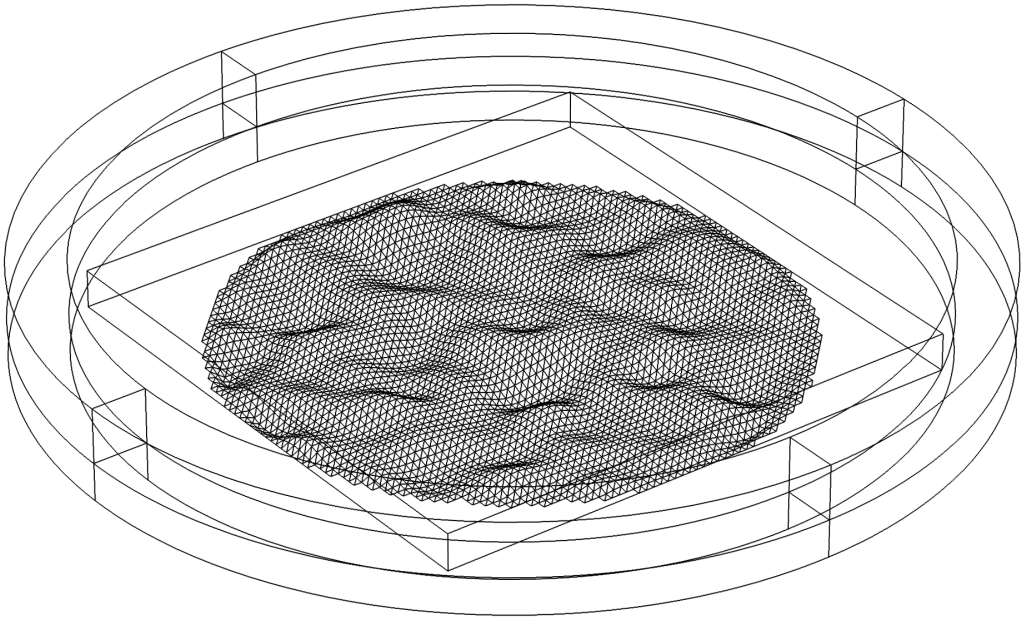

Figure 5.1: Geometry used for 3D FEM simulation. The circular patch in the center is the scattering surface located at the bottom of a rectangular prism inset in a cylinder, all of which comprise the computational domain. Absorbing layers are placed outside of and above this domain. Rigid boundary conditions ($\frac{\partial p}{\partial n} = 0$ where n is the normal vector on the boundary) prescribed on all exterior boundary conditions except the bottom of the computation domain, on which a pressure-release boundary condition ($p = 0$) is prescribed.

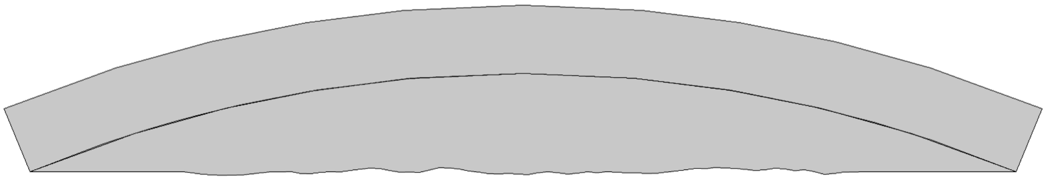

Figure 5.2: Geometry used for 2D FEM simulation. The rough interface at the bottom acts as a scatterer, where a pressure-release ($p = 0$) boundary condition is applied. In order to reduce sharp edges, a curved top boundary is prescribed with a bordering absorbing layer. Rigid boundary condition ($\frac{\partial p}{\partial n} = 0$ where n is the normal vector on the boundary) applied on all other exterior boundaries.

putational domain, reducing solution time. As mentioned earlier, unlike the mesh-like nature of the rough surface in 3D, it looks like a simple perturbation of the bottom interface in 2D.

5.2 Mesh Generation

Mesh generation describes a process of creating a set of connected nodes that form elements. A basis function is prescribed to each element and the differential equation is solved so that the overall error is minimized using the Galerkin method. Elements can have a number of different shapes, but the most common elements for 2D modeling are triangular and quadrilateral elements. For 3D modeling, they are tetrahedral (with triangular faces) and hexahedral (with quadrilateral faces) elements. Due to the irregular facets produced by and required by rough surfaces, triangular and tetrahedral elements were used. A sample 2D mesh for the FEM model used in this work is shown in Fig. 5.2.

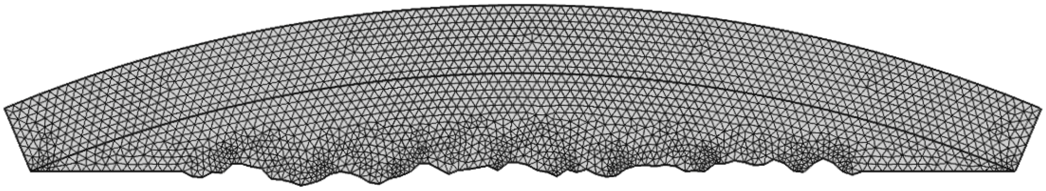

Figure 5.3: Sample 2D mesh for FEM model

The mesh is designed to be able to resolve features in the geometry including all boundaries. In order to well-approximate a curved surface, it requires a smaller discretization. The mesh generation software dynamically sets the size of the elements in order to meet certain criteria such as maximum element size, minimum element size, maximum element growth rate, curvature factor, and resolution of narrow regions. Furthermore, all points are made into nodes and all boundaries, including the rough surface, are meshed fine enough to fully describe the prescribed geometry.

A sample 3D mesh is given in Fig. 5.4. It is difficult to visualize the connectivity of the nodes in a 3D mesh, so only half of the mesh elements are shown.

5.3 Physics and Parameter Definition

In COMSOL Multiphysics, the different differential equations being solved are packaged as different "physics." Each of these "physics" have an associated weak formulation that is hard-coded into the software by the de-

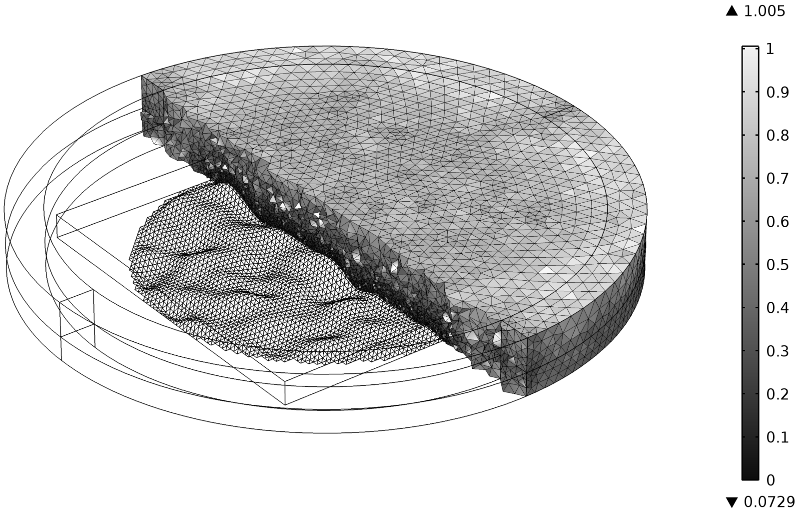

Figure 5.4: Sample 3D mesh for FEM model, brightness corresponds to relative element size

velopers. For this work, the only physics being used is known in COMSOL as “pressure acoustics,” whose governing equation is the wave equation in the time domain or the Helmholtz equation in the frequency domain [18]. This work uses the latter in the form

$$\nabla \cdot \left(-\frac{1}{\rho_0} \left(\nabla p - \mathbf{q} \right) \right) - \frac{\omega^2}{\rho_0 c^2} p = \mathbf{Q}, \tag{5.1}$$

where $\mathbf{q}$ and $\mathbf{Q}$ are the dipole and monopole source terms, respectively, ρ_0 is the equilibrium density of the medium, c is the sound speed, $\omega = 2\pi f$ is the angular frequency of the wave, and p is the acoustic pressure. For this work, ρ_0 was constant and no explicitly defined dipole or monopole terms were used. A monopole term is used implicitly when applying the incident wave, as discussed later in this section. Equation 5.1 simplifies to the well known form

$$\left(\nabla^2 + k^2 \right) p = 0. \tag{5.2}$$

The weak formulation for the finite element method requires the use of an approximating space for the test and trial functions. For this work, the approximating space is defined as the linear combination of piecewise LaGrange polynomial basis functions that span a local set of elements. These basis functions are also prescribed to be *nodal*, meaning that their value is unity at a single node or vertex and zero at all other nodes. This allows for convenient polynomial interpolation and leads to a well-conditioned matrix for solving [17]. For general FEM in contrast with spectral element methods, the order of these basis functions are kept low. For this work, these basis function were quadratic (order = 2).

Boundary conditions can be enforced in the weak formulation (weakly) or through manipulation of the stiffness matrix discussed in Sec. 5.4 (strongly). The pressure release boundary condition on the rough surface, a Dirichlet condition, is enforced strongly whereas the rigid boundary condition on all other exterior boundaries, a Neumann condition, is enforced weakly. Interior boundaries (boundaries between subdomains within the model) maintain continuity of acoustic pressure, imposed implicitly.

The incident wave was prescribed using what COMSOL calls a "Background Pressure Field." Mathematically, this is implemented by defining the total pressure $p = p_b + p_s$, where p_b is the background pressure field and p_s is the scattered pressure being solved for. Substituting this new definition of p into Eq. 5.2 gives

$$\left(\nabla^2 + k^2\right) p_s = -\left(\nabla^2 + k^2\right) p_b, \tag{5.3}$$

which creates an equivalent monopole source term that excites the desired background pressure field.

The incident wave prescribed was a modified Gaussian plane wave [11, 19]. This was used in order to eliminate edge effects. In 3D, this is given by

$$p_i(\mathbf{r}) = \exp\left(-i\mathbf{k_i}\cdot\mathbf{r}[1+w]\right)\exp(-t), \tag{5.4}$$

where $t = t_x + t_y$,

$$t_x = \frac{(\cos\theta_g x + \sin\theta_g z)^2}{g^2\cos^2\theta_g}, \tag{5.5}$$

$$t_y = \frac{y^2}{g^2}, \tag{5.6}$$

$$w = \frac{1}{k^2}\left[\frac{2t_x - 1}{g^2\cos^2\theta_g} + \frac{2t_y - 1}{g^2}\right], \tag{5.7}$$

and g is the beam waist. In 2D, this is given by

$$p_i(\mathbf{r}) = \exp(i\mathbf{k}_i\cdot\mathbf{r}[1+w(\mathbf{r})])\exp(-b^2(\mathbf{r})/g^2), \tag{5.8}$$

where

$$w(\mathbf{r}) = [2b^2(\mathbf{r})/g^2 - 1]/(kg\cos\theta_g)^2, \tag{5.9}$$

$$b(\mathbf{r}) = x - z\tan\theta_g. \tag{5.10}$$

These modified Gaussian-tapered plane waves provide a Gaussian tapering on the mean plane of the surface while adequately satisfying the Helmholtz equation for propagation. The tapering parameter g was set to one-sixth the length of the rough surface in accordance with [1]. It is instructive to note that unlike the simple incident plane wave (Eq. 3.2), the intensity is not unity and must be calculated before scattering strength can be computed. This is done numerically using trapezoidal integration on the mean plane. The grazing angle of the incident field θ_i was fixed to 55 degrees for this work.

The size of the mesh is constrained by the physics. For the Helmholtz equation, it is necessary to be able to resolve the phase of the acoustic wave properly. This requires that the mesh size B be much smaller than a wavelength λ. Specifically, COMSOL recommends a mesh size $B = \lambda/M$ where $5 < M < 10$ [18]. The error for the finite element method goes to zero as the mesh becomes finer. Put another way, the finite element method converges to the exact solution given an adequately fine mesh. Calculations for this work were constructed with a maximum element size of $\lambda/7$.

Furthermore, an effective anechoic environment is required for the model domain. This requires the use of a mechanism to remove energy from the system at outer boundaries. Early attempts use a gradually increasing attenuation to create an absorbing layer that reduces the sound field to near zero at the boundary and eliminates any reflections. However, reflection from an attenuating medium is possible and the gradual change requires a thick layer to effectively attenuate the wave. Instead, perfectly matched layers (PMLs) are used. Instead of using an attenuating medium, a complex coordinate scaling is used that attenuates the wave [20]. This allows for the layer to have an identical impedance to the propagating medium yet still facilitate exponential attenuation. This is implemented such that scaling orthogonal to the boundary between the PML and a non-PML subdomain (the inner boundary) is given by [18]

$$\xi' = \operatorname{sign}(\xi - \xi_0)\,|\xi - \xi_0|^n\,\frac{L}{\delta\xi^n}(1-i), \tag{5.11}$$

where ξ is the coordinate normal to the inner boundary, ξ' is the scaled coordinate that is used instead of the actual coordinate during finite element calculations, ξ_0 is the value of ξ at the inner boundary, $\delta\xi$ is the geometric width of the PML, $L/\delta\xi$ is the PML scaling factor, and n is the PML order. For this work, $L/\delta\xi = 1$, $n = 1$, and $\delta\xi = \lambda$ (the acoustic wavelength).

5.4 Solution

The power of the finite element method formulation is that it produces an algebraic system that can be solved easily using existing techniques. Specifically, test and trial function product integrals can be computed element-by-element and coupled algebraically. The problem is then reduced to the form

$$A\mathbf{x} = \mathbf{b}, \tag{5.12}$$

where A is known as the stiffness matrix, $\mathbf{x}$ is the vector of unknowns that make up the degrees of freedom, and $\mathbf{b}$ is the load vector that contain source terms that are not dependent on $\mathbf{x}$. Furthermore, the pressure-release condition on the interface, as mentioned in the previous subsection, is enforced in this matrix. This is done simply by setting the components of $\mathbf{x}$ that represent vertices on the interface to 0 and removing the corresponding terms and equations from the system [17]. Lastly, the stiffness matrix is also sparse, symmetric, and positive definite, characteristics that are computationally advantageous.

After constructing the condensed linear system, it can be solved directly through LU factorization or similar algorithm or an iterative method (e. g. generalized minimal residual method, GMRES). For this work, a direct solver is used that implements the LU factorization routine in a computationally efficient way for multiple processors and nodes. Specifically, the Multifrontal Massive Parallel Sparse Direct Solver (MUMPS) was used to solve the finite element matrix equation [18]. The calculations for the results presented in Chapter 7 were performed using the Texas Advanced Computing Center (TACC) high performance cluster Lonestar 4.

5.5 Boundary Integral

In the final step, the Helmholtz-Kirchhoff integral is calculated on the rough surface [18]. Specifically, it is evaluated in the far-field. This is done in order to determine the far-field intensity and, therefore, the scattering strength. The pressure in this regime can be evaluated using a boundary integral on the rough surface. The precise form of this integral is given as

$$p_{\mathrm{far}}(\mathbf{r}) = \frac{1}{4\pi}\int_S \frac{e^{-ik|\mathbf{r}_0-\mathbf{r}|}}{|\mathbf{r}_0-\mathbf{r}|}\left(\nabla p(\mathbf{r}_0) + p(\mathbf{r}_0)\frac{1+ik|\mathbf{r}_0-\mathbf{r}|}{|\mathbf{r}_0-\mathbf{r}|^2}(\mathbf{r}_0-\mathbf{r})\right)\cdot \mathbf{n}\, dS, \tag{5.13}$$

where $\mathbf{r}_0$ is a point on the rough surface, $\mathbf{r}$ is the receiver point, and $\mathbf{n}$ is the normal vector on the rough surface. The subscript ‘far’ refers to ‘far-field.’

In order to compare with other models, it is necessary to calculate the scattering cross section. This was defined earlier in Eqs. (4.18) and (4.17). An alternate form is given by [11, 1]

$$\sigma_{3\mathrm{D}}(\theta_i, \theta_s, \phi_s) = \frac{|p_{3\mathrm{D}}(\theta_s, \phi_s)|^2 r^2}{E_{3\mathrm{D}}}, \tag{5.14}$$

for 3D space and

$$\sigma_{2\mathrm{D}}(\theta_i, \theta_s) = \frac{|p_{2\mathrm{D}}(\theta_s)|^2 r}{E_{2\mathrm{D}}}, \tag{5.15}$$

for 2D space, where $E_{2\mathrm{D}}$, $E_{3\mathrm{D}}$ are the sound flux through a surface A per unit time and $p_{2\mathrm{D}}$, $p_{3\mathrm{D}}$ are the field pressures at a range r in the far-field at angles θ_s and ϕ_s.

As mentioned before, the finite element method converges to the exact solution as the discretization becomes finer. Due to this property, the FEM model was used as a benchmark for both 2D and 3D scattering. The result of applying the transdimensional factors discussed in Chapter 6 to 2D FEM results are compared to 3D FEM results in Chapter 7.

Chapter 6

Transdimensional Factors

In this chapter, three factors are derived that provide a means of comparing two-dimensional scattering to three-dimensional scattering. The first is a spreading factor derived from the analytical comparison of reflections from 2D and 3D surfaces. The second is a perturbative factor that allows for handling isotropically rough 3D surfaces. And the last is a combined factor that takes into account the strengths of both the spreading and perturbative factors.

6.1 Spreading Factor

A factor has been developed that relates 2D and 3D scattering by comparing the scattering cross-section from two flat surfaces. It has been shown that there is a simple algebraic relation between the solutions to these problems by Sumedh Joshi in his master's degree work [1]. A brief derivation of this factor is presented here; the next three subsections present scattering from a plane piston in 3D, scattering from a line source in 2D, and their ratio, respectively.

An important thing to consider is a physical intuition of what this approach accounts for and what it does not. Specifically, since the formulation compares two *flat* cases, there is no accounting for changes in roughness. However, it does well to capture effects of a difference in the source condition.

6.1.1 Shaded Plane Piston in Three-Dimensional Space

The flat piston in 3D space is analogous to the 3D scattering problem off of a 2D surface. The Fraunhofer approximation to the Rayleigh integral is given by

$$p_{\text{flat,3D}}(x, y, z) = -\frac{ik\rho_0 c_0}{2\pi}\frac{e^{ikr}}{r}\int_{-\infty}^{\infty}\int_{-\infty}^{\infty} u_0(x_0, y_0) e^{-ik(xx_0+yy_0)/r} dx_0 dy_0, \quad (6.1)$$

where ρ_0 is the bulk density of the water, c_0 is the sound speed of the water, k is the natural wavenumber defined as $2\pi f/c_0$, f is the frequency of the source, and r is the distance from the origin to the field point $\sqrt{x^2 + y^2 + z^2}$. This form is specific to the far-field for a velocity source with distribution $u_0(x_0, y_0)$ in the source plane $z = 0$ radiating into the half space $z > 0$.

Recognizing that Eq. (6.1) can be formulated as a spatial Fourier transform, it can be represented as

$$p_{\text{flat,3D}}(r, \theta, \phi) = -\frac{ik\rho_0 c_0}{2\pi}\frac{e^{ikr}}{r} U_0(k\alpha, k\beta), \quad (6.2)$$

where $U_0(k_x, k_y) = \mathcal{F}\{u_0(x_0, y_0)\}$, $\alpha = \cos\phi\cos\theta$, $\beta = \sin\phi_s \cos\theta_s$, θ_s is the grazing angle of the field point relative to the source plane, and ϕ_s is the azimuth of the field point. Linear phase shading is then applied to steer the specular direction of scattering and Gaussian shading to match the beam [11].

This yields the following analytical form [1]:

$$p_{\text{flat,3D}}(r,\theta_s,\phi_s) = -\frac{1}{2}ik\rho_0 c_0 u_0 g^2 \frac{e^{ikr}}{r} e^{-k^2g^2[(\alpha-\cos\theta_i)^2+\beta^2]/4}. \tag{6.3}$$

6.1.2 Shaded Line Source in Two-Dimensional Space

The line source in 2D space is analogous to 2D scattering off of a rough interface. The 2D Rayleigh integral is of the form

$$p_{\text{flat,2D}}(x,z) = \frac{ik\rho_0 c_0 u_0}{2}\int_{-\infty}^{\infty} e^{-x_0^2/g^2} H_0^{(1)}\left(k\sqrt{(x-x_0)^2+z^2}\right) dx_0, \tag{6.4}$$

where $H_0^{(1)}$ is the zeroth-order Hankel function of the first kind. Substituting the asymptotic form into Eq. (6.4),

$$p_{\text{flat,2D}}(x,z) = \frac{ik\rho_0 c_0 u_0}{2}\int_{-\infty}^{\infty} e^{-x_0^2/g^2}\sqrt{\frac{2}{\pi kR}}e^{ikR-i\pi/4}dx_0, \tag{6.5}$$

where $R = \sqrt{(x-x_0)^2+z^2}$. A binomial expansion of $R = r[1 - xx_0/r^2 + x_0^2/2r + \cdots]$ is performed where $r = \sqrt{x^2+z^2}$ and substituted into Eq. (6.5). Retaining first-order amplitude terms and second-order phase terms,

$$p_{\text{flat,2D}}(x,z) = \frac{k\rho_0 c_0 u_0}{\sqrt{2\pi}} e^{-i\pi/4}\frac{e^{ikr}}{\sqrt{kr}}\int_{-\infty}^{\infty} e^{-x_0^2/g^2} e^{-ik\frac{x}{r}x_0}dx_0. \tag{6.6}$$

This form is analogous in 2D to Eq. (6.1) from the previous subsection. As before, this integral is cast as a Fourier transform in the source plane:

$$p_{\text{flat,2D}}(x,z) = \frac{k\rho_0 c_0 u_0 g}{\sqrt{2\pi}} e^{-i\pi/4}\frac{e^{ikr}}{\sqrt{kr}}\mathcal{F}_x\{e^{-x_0^2/g^2}\}. \tag{6.7}$$

Applying linear phase shading and Gaussian shading on the line source yields [1]

$$p_{\text{flat,2D}}(x,z) = \frac{k\rho_0 c_0 u_0 g}{\sqrt{2}} e^{-i\pi/4}\frac{e^{ikr}}{\sqrt{kr}} e^{-k^2g^2(\cos\theta_s-\cos\theta_i)^2/4}. \tag{6.8}$$

6.1.3 Ratio of Scattering Cross Section

The transdimensional factors are meant to be applied to scattering cross section, which is nondimensional for rough surface scattering (scattering cross section for infinite surfaces is defined per unit area). Substituting Eq. (6.8) into Eq. (5.15) and Eq. (6.3) into Eq. (5.14) and setting $\phi_s = 0$ gives

$$\sigma_{\text{flat,3D}}(\theta_i, \theta_s) = \frac{(k\rho_0 c_0 u_0 g^2/2)^2 e^{-k^2 g^2[\cos\theta_s - \cos\theta_i]^2/2}}{E_{\text{3D}}}, \tag{6.9}$$

$$\sigma_{\text{flat,2D}}(\theta_i, \theta_s) = \frac{(\sqrt{k}\rho_0 c_0 u_0 g/\sqrt{2})^2 e^{-k^2 g^2[\cos\theta_s - \cos\theta_i]^2/2}}{E_{\text{2D}}}. \tag{6.10}$$

Dividing Eq. (6.9) by Eq. (6.10) arrives at the spreading factor [1]

$$T_{\text{S}} = \frac{\sigma_{\text{flat,3D}}}{\sigma_{\text{flat,2D}}} = \frac{1}{2} k g^2 \frac{E_{\text{2D}}}{E_{\text{3D}}}, \tag{6.11}$$

where the subscript S refers to ‘spreading.’

This factor provides a means of quantifying the differences between the 2D and 3D reflection problem. However, it does *not* include anything about the character of the roughness. This is why this term was named the spreading factor. It incorporates the nature of how sound scatters from surfaces between two and three dimensions, which is essentially a change in geometrical spreading.

6.2 Perturbative Factor

Spreading is not the only difference between 2D and 3D scattering. The cumulative effects of changing from 2D to 3D can be approximated by the ratio of the 3D perturbation theory scattering cross section to the 2D scattering cross section:

$$T_{\mathrm{P}}(\theta_s) = \frac{\sigma_{\mathrm{pt,3D}}(\theta_s)}{\sigma_{\mathrm{pt,2D}}(\theta_s)}, \tag{6.12}$$

where the subscript P refers to ‘perturbative.’ Substituting Eqs. (4.28) and (4.29) into Eq. (6.12) gives

$$T_{\mathrm{P}}(\theta_s) = \frac{4k^4 \cos(\theta_i)\cos(\theta_s) W_2(kA)}{4k^3 \cos(\theta_i)\cos(\theta_s) W_1(kA)}, \tag{6.13}$$

which simplifies to

$$T_{\mathrm{P}}(\theta_s) = k\frac{W_2(kA)}{W_1(kA)}, \tag{6.14}$$

where k is the wavenumber and W_1, W_2 are the power spectra for 1D, 2D surfaces, respectively, and $kA = k(\cos\theta_g - \cos\theta_s)$ is the difference of horizontal wavenumber of the incident and scattered waves. In comparison to the spreading factor, the isotropic roughness factor is statistical, and only applies to an ensemble averages of rough surfaces. Furthermore, it may requires the surface be within the range of validity of perturbation theory. This requirement is discussed further in Chapter 7. Unlike the spreading factor derived in Section 6.1, this factor provides an angle-dependent coefficient as well as incorporating the change in roughness from 1D to 2D surfaces.

For von Karman spectra, substituting Eqs. (2.3) and (2.2) into Eq. (6.14) gives

$$T_{\mathrm{P,VK}}(\theta_s) = \frac{\Gamma\left(\frac{\gamma_2}{2}\right)}{\sqrt{\pi}\,\Gamma\left(\frac{\gamma_2 - 1}{2}\right)} \frac{k}{\sqrt{K^2 + K_0^2}}, \tag{6.15}$$

where the subscript VK refers to the von Karman power spectrum for which it is applicable. For Gaussian surfaces, substituting Eqs. (2.8) and (2.7) into

Eq. (6.14) gives

$$T_{\mathrm{P,G}} = \frac{kl}{\sqrt{4\pi}}, \tag{6.16}$$

where the subscript G refers to the Gaussian power spectrum. Note that for gaussian surfaces, the perturbative factor is not dependent on scattered angle.

6.3 Combined Factor

It has been shown that the spreading factor works well near the specular peak [1, 21]. A comparison of the spreading factor (Eq. (6.11)) and the perturbative factor (Eq. (6.11)) is shown in Fig. 6.1. In the specular direction (55 degrees), the perturbative factor rapidly approaches a maximum. It can be reasoned that an appropriate transdimensional factor should not exceed

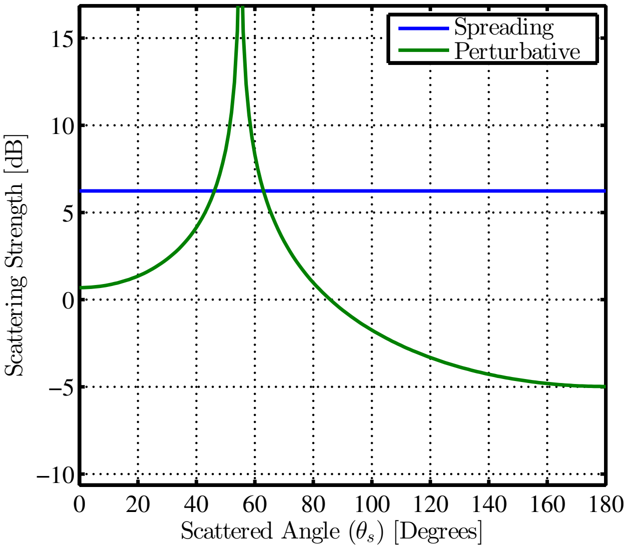

Figure 6.1: Comparison between spreading and perturbative transdimensional factors for the VK dataset (see Section 7.1)

the spreading factor in the specular direction. A new combined factor is then developed from the minimum of the spreading and perturbative factors at each scattering angle:

$$T_{\mathrm{C}}(\theta_s) = \min\left\{k\frac{W_2(kA)}{W_1(kA)}, \frac{1}{2}kg^2\frac{E_2}{E_3}\right\}, \tag{6.17}$$

where the subscript C refers to ‘combined.’

Chapter 7

Results

This chapter presents the results of conducting simulations using perturbation theory and finite elements, described in Chapters 4 and 5, with a variety of roughness statistics that are derived from published papers. Results are presented in graphs of scattering strength (in dB) vs. scattered angle (in degrees). Scattering strength is defined as $10\log_{10}\sigma$ where σ is the scattering cross section in 2D or 3D, and scattered angle is the angle θ_s defined in Chapter 3 where $\theta_s = 0$ is the $+x$ direction, $\theta_s = 90$ is the $+y$ direction, and $\theta_s = 180$ is the $-x$ direction. The parameters tested are as follows: three von Karman spectra designated VK, VK5, and VK20; and three Gaussian spectra designated G2, G3, and G4.

7.1 von Karman Spectra

These parameter sets are variations on those used in the paper "A Geoacoustic Bottom Interaction Model (GABIM)" [22]. Referred to as VK, VK5, and VK20, these parameters use the von Karman spectrum for which they are named (see Eqs. (2.4) and (2.5) in Section 2.1). The VK parameters are those used to generate Fig. 2 in Ref. 22 simplified to a single incident angle with multiple scattered angles, known as the multistatic case. A summary of these parameters is given in Table 7.1.

Table 7.1: Summary of Parameters for VK Case

Parameter	Value
γ_2	3.0
w_2	0.0004 $\mathrm{m}^{4-\gamma_2}$
K_L	0.01 m^{-1}

The effects of applying all three factors—spreading (Eq. (6.11)), perturbative (Eq. (6.14)), and combined (Eq. (6.17))—to 2D FEM simulations using the VK parameters are shown in Fig. 7.1 with the 3D FEM results provided as a benchmark for the correct response.

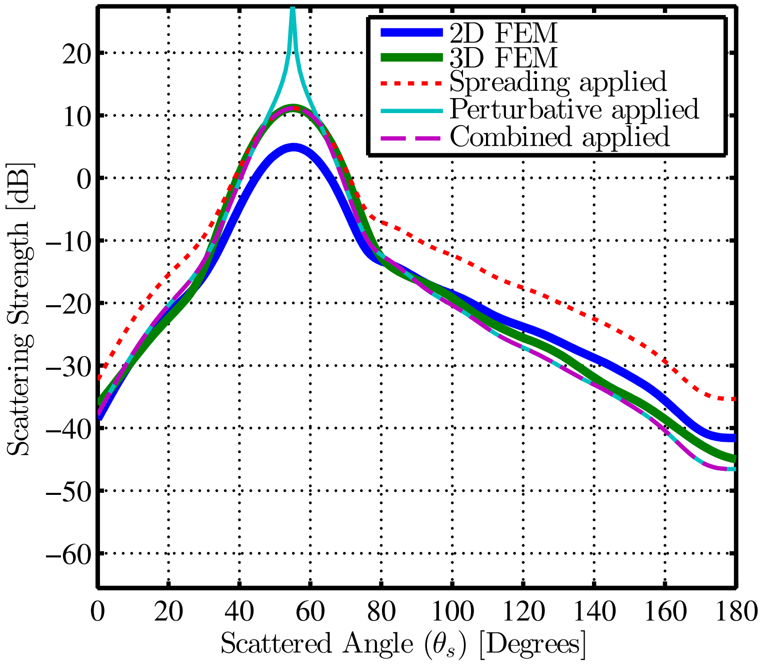

Figure 7.1: Comparison between three factors applied to 2D FEM results, compared to 3D FEM results, for VK data set

Consistent with previous work using the Kirchhoff approximation [21], the usefulness of the spreading transdimensional factor is limited to close to the specular peak, because the spreading factor is constant with scattered angle. At the specular peak, however, it performs very well.

The perturbative factor provides useful scaling of the 2D results away from the specular direction. While not exact even away from specular, this factor provides appropriate scaling (i.e. scales up when 2D scattering is of lower magnitude than 3D scattering and vice versa). Due to the strengths of each of the other factors, the combined factor performs best, almost scaling properly throughout the scattered angles.

In order to understand the effect of the perturbative factor, it is useful to compare the computed finite element results with perturbation theory results. These results are shown in Fig. 7.2. Whereas Fig. 7.1 compares the effect of applying the factors to 2D FEM to 3D FEM, Fig. 7.2 compares 2D FEM without the factors to 2D perturbation theory and 3D FEM directly to 3D perturbation theory, showing the extent to which perturbation theory is valid. For the VK parameter set, perturbation theory performs very well away from specular. This is consistent with the performance of the perturbative factor.

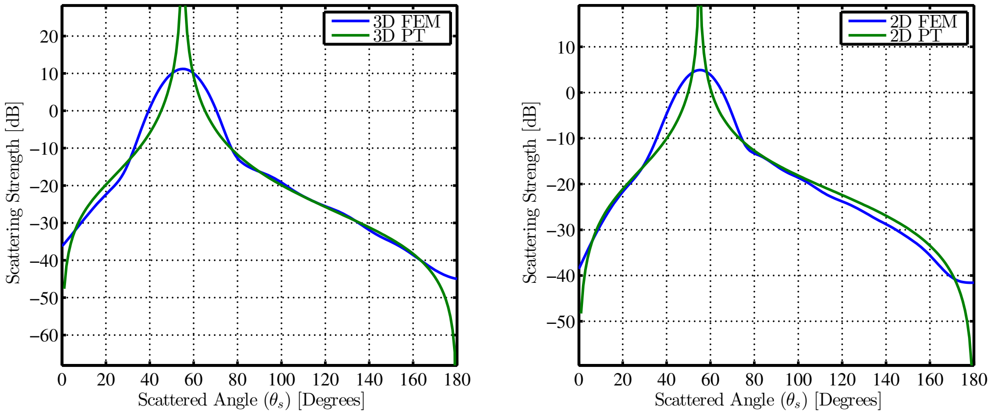

(a) 3D

(b) 2D

Figure 7.2: Comparison of FEM with Perturbation Theory for VK parameters

In order to test perturbation theory and the perturbative factor, the spectral strength of the power spectrum used previously has been increased five-fold ($w_2 = 0.002$) hence the name VK5, which raises the root-mean-square height of the generated surfaces without changing the relative dominance of spatial frequencies. This is equivalent to multiplying the entire power spectrum by 5. Results are shown in Fig. 7.3.

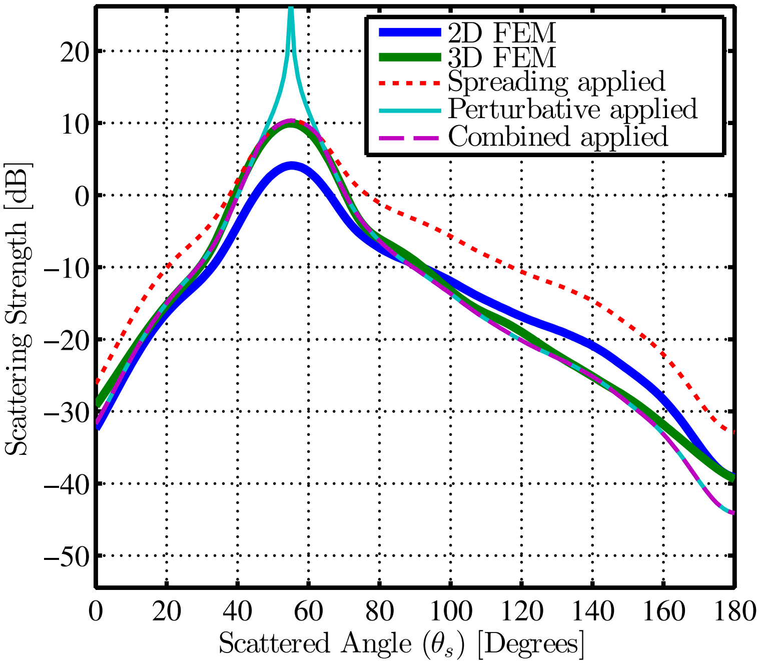

Figure 7.3: Comparison between three factors applied to 2D FEM results, compared to 3D FEM results, for VK5 data set

Results are consistent with the observations made for the unmodified VK roughness parameters. Again, perturbation theory captures the behavior of the scattering well, as evidenced by the curves in Fig. 7.4.

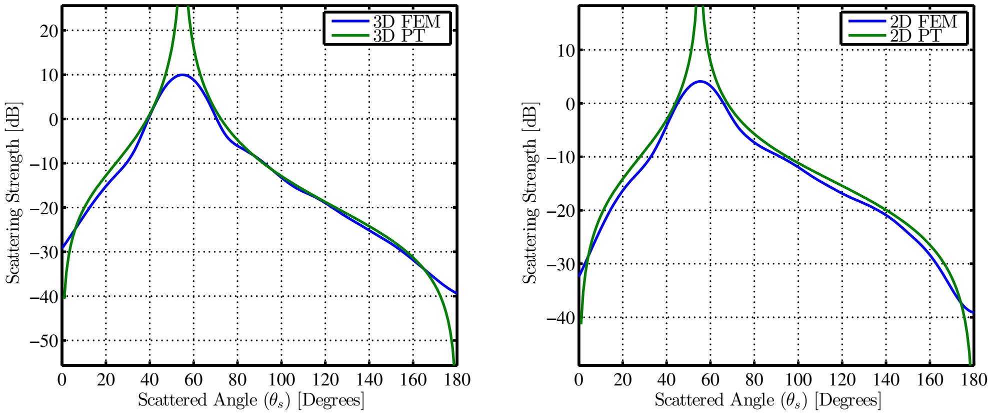

(a) 3D

(b) 2D

Figure 7.4: Comparison of FEM with Perturbation Theory for VK5 parameters

In order to study the effects of higher roughness on the efficacy of the transdimensional factors, the spectral strength was increased by 20× ($w_2 = 0.008$). Surprisingly, the performance of the factors for VK20 are quite similar to the performance seen in the unmodified VK and VK5 parameter sets, as seen in Fig. 7.5.

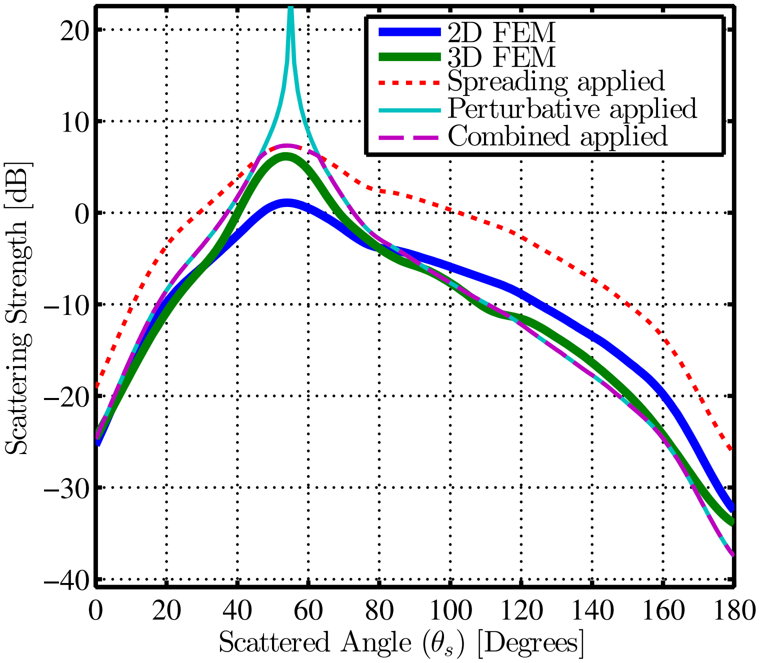

Figure 7.5: Comparison between three factors applied to 2D FEM results, compared to 3D FEM results, for VK20 data set

In this case, perturbation theory is inconsistent with the FEM solutions, as seen in Fig. 7.6. Perturbation theory predicts fairly well far from the specular peak but fails to conform to the general shape within 40 degrees of the specular direction in both the 2D and 3D scattering cases. This seems to indicate that the transdimensional factors are fairly robust against the validity of perturbation theory.

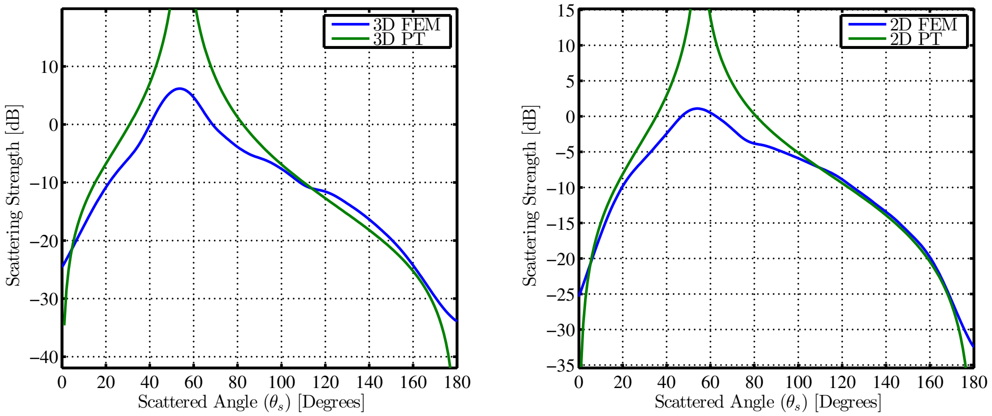

(a) 3D

(b) 2D

Figure 7.6: Comparison of FEM with Perturbation Theory for VK20 parameters

7.2 Gaussian Spectra

Since the validity of perturbation theory is well-known for Gaussian surfaces, it is instructive to look at the performance of the transdimensional factors with the parameters of [2]. They are chosen to adequately represent varying levels of validity for first-order perturbation theory, shown in Fig. 7.7. A summary of the parameters tested are given in Table 7.2.

Table 7.2: Summary of Gaussian roughness parameters used in this thesis

Parameter Set	kl	kh
G2	2.6	0.52
G3	4.5	0.69
G4	10.0	1.03

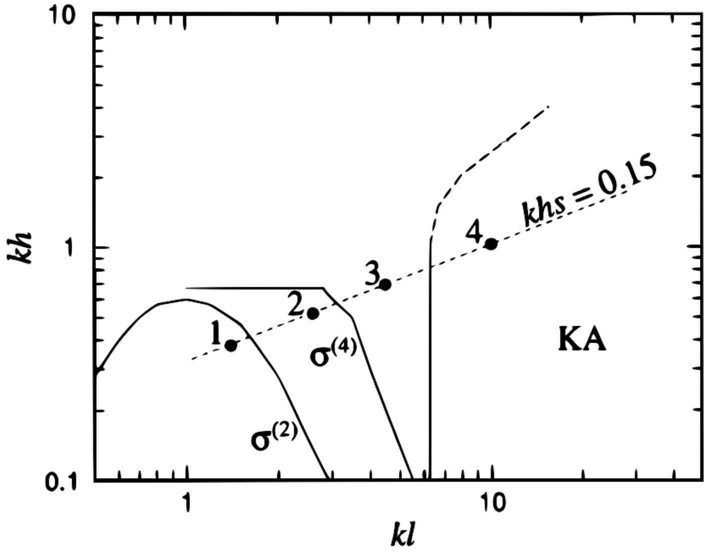

Figure 7.7: Region of validity for first-order perturbation theory $\sigma^{(2)}$, next-order perturbation theory $\sigma^{(4)}$, and the Kirchhoff Approximation (KA). Superimposed are the locations of the numerical examples. *khs* is the Fresnel number given by the product of the wavenumber, rms height, and rms slope. Adapted from [2].

Figure 7.8 shows the effects of the transdimensional factors on the 2D results. It's of interest to point out the differences in the nature of scattering from a surface with a Gaussian surface versus scattering from a surface with a von Karman spectrum. The specular peak is more pronounced and rises well from the background whereas the incoherent energy seems to conform to a smooth bell-shaped curve. Also, recall that the perturbative factor for Gaussian surfaces is constant. Note that the scattering in 2D and 3D for these parameters are already similar. For the majority of the scattered angles, especially away from specular, the curves agree. Furthermore, the perturbative factor is inappropriate for these surfaces. The correction itself is a -2.7 dB offset. On the other hand, the spreading factor accurately predicts the level of the specular peak. Unfortunately, since the combined factor is the minimum of the perturbative and spreading factors, the combined factor is unable to incorporate the spreading factor at all.

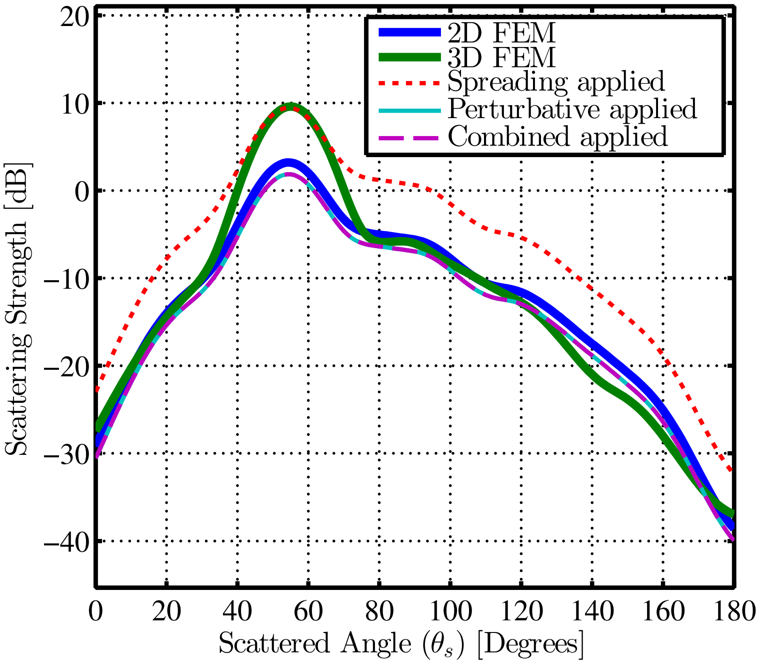

Figure 7.8: Comparison between three factors applied to 2D FEM results, compared to 3D FEM results, for G2 data set

The comparison of perturbation theory with the FEM results are shown in Fig. 7.9. The two curves are in general agreement, though perturbation theory does miss some behavior for these parameters. This result is expected, as G2 uses parameters that are known to reside just outside the region of validity for first-order perturbation theory, shown in Fig. 7.7.

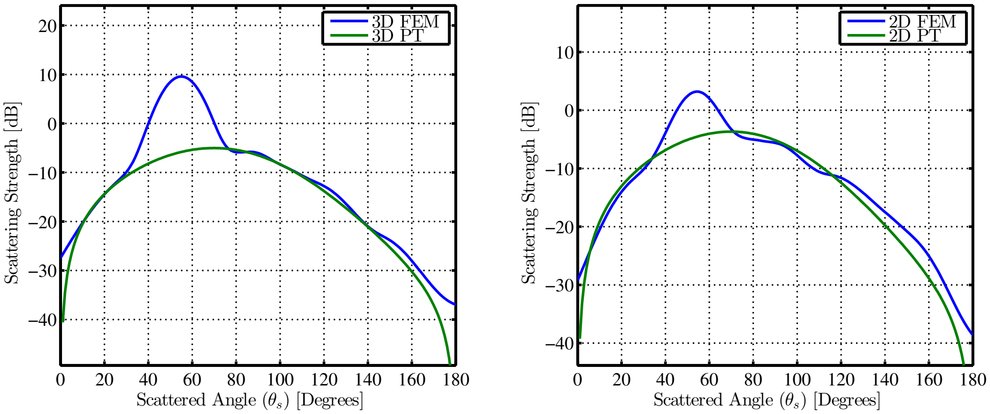

(a) 3D

(b) 2D

Figure 7.9: Comparison of FEM with Perturbation Theory for G2 parameters

The next case is in what Kaczkowski calls the ‘gap region’ [2]. These parameters are in the region of validity of neither perturbation theory nor the Kirchhoff approximation. The performance of the transdimensional factors are similar to that of G2, as shown in Fig. 7.10. However, the perturbative factor predicts a 2 dB increase. Although it does not approximate the 3D results well, the factor seems to remain conservative when viewed in the context of Fig. 7.11. The spreading factor again correctly predicts the level of the specular peak.

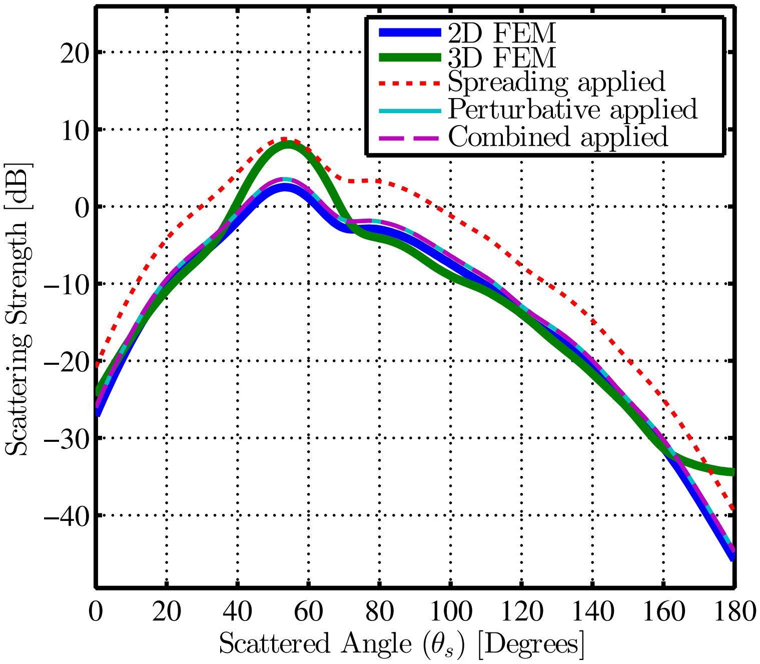

Figure 7.10: Comparison between three factors applied to 2D FEM results, compared to 3D FEM results, for G3 data set

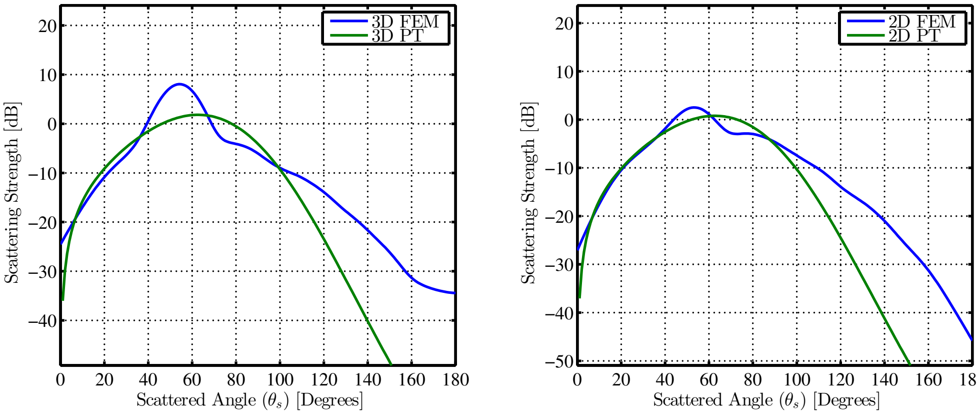

(a) 3D

(b) 2D

Figure 7.11: Comparison of FEM with Perturbation Theory for G3 parameters

This last case is perhaps the most interesting example presented in this work. Similar to the other cases taken from the paper by Kaczkowski and Thorsos, the 2D and 3D scattering models are almost equivalent, though there seems to be some sort of artifact at high grazing angles in the 3D FEM results. The veracity of the 3D FEM results in this region is questionable due to its uncharacteristic increase, which may be caused by the discretization. When viewed in concert with Fig. 7.13, the results of the application of the factor in Fig. 7.12 are almost acceptable. For this case, the perturbative factor predicts a 2.8 dB increase. Furthermore, the spreading factor does not work at any angle either.

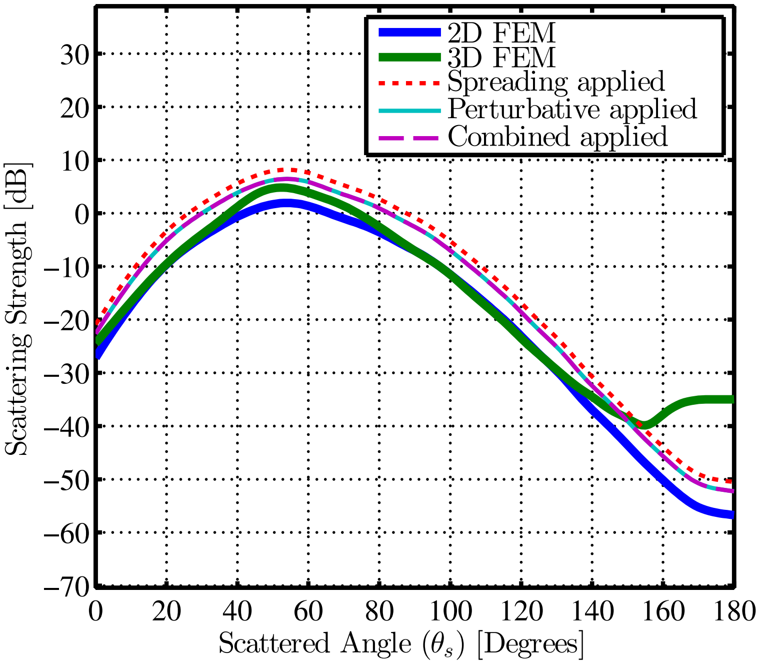

Figure 7.12: Comparison between three factors applied to 2D FEM results, compared to 3D FEM results, for G4 data set

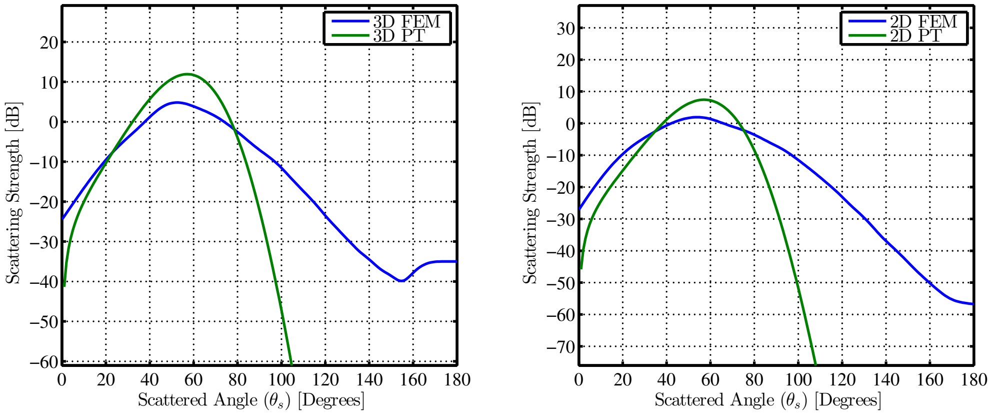

(a) 3D

(b) 2D

Figure 7.13: Comparison of FEM with Perturbation Theory for G4 parameters

Chapter 8

Conclusions

Direct numerical simulation of acoustic scattering is a time-consuming and cumbersome task. However, the necessity of accurate and reliable estimation of seafloor scattering is undeniable. In the isotropic approximation of seafloor roughness, two-dimensional simulation should be adequate to fully characterize three-dimensional scattering. However, the results cannot be used from these two-dimensional models directly. This thesis presents a method for comparison between these models and three-dimensional scattering results.

8.1 Summary

Roughness spectra are described in Chapter 2. This work used both the von Karman and Gaussian roughness spectra in order to model the seafloor. The von Karman spectrum is known to adequately represent true seafloors whereas the Gaussian spectrum provides simplicity and literary precedence for studies of mathematical validity [3]. Both spectra were used as inputs into physical models that approximate the situation described in Chapter 3, which isolates scattering within the locus of effects that comprise underwater acoustic propagation. The models used in this work were first-order small perturbation theory, presented in Chapter 4, and the finite element method, presented in Chapter 5. Perturbation theory is a computationally simple model that provides a formally-averaged statistical calculation of scattering from slightly rough surfaces whereas the finite element method is a direct numerical simulation of the scattering problem that uses domain truncation techniques and the Monte Carlo method to generate similarly statistical results [12, 17]. While perturbation theory is only valid for a subset of rough surfaces, the finite element method converges to the exact solution for all cases (see Chapter 5). Because of this behavior, the finite element model was used as the benchmark model for this work.

Transdimensional factors that relate 2D and 3D scattering are presented in Chapter 6. The first is referred to as the spreading factor and is adopted from [1]. It captures the effective difference between coherent spreading from the reflection of a plane wave off a flat surface. The second is referred to as the perturbative factor and is derived from the ratio of perturbation theory solutions in two and three dimensions. This factor is an attempt at characterizing the effects of roughness on the incoherent fields present in 2D and 3D. Unlike the spreading factor, which is constant with scattered angle, the perturbative factor is, like perturbation theory itself, dependent on the difference between the horizontal wavenumbers of incident and scattered waves. Lastly, a third transdimensional factor was created by taking the minimum of the other two factors. This relation was determined by observation.

The application of these factors to the finite element models is presented in Chapter 7. Additionally, comparison between perturbation theory and the finite element models are shown. For von Karman spectra, the combined factor effectively provides the 3D effects of scattering, successfully converting 2D scattering model results to acceptable 3D results. This is especially true for the low roughness case referred to as VK. In the VK5 case, where the spectral strength from the VK parameter set was increased 5×, and the VK20 case, where the spectral strength was increased 20×, the combined transdimensional factor displayed robustness, though its applicability with greater roughness is less concrete. However, in all von Karman parameter sets used, perturbation theory showed consistent agreement with finite elements. These results are presented in Section 7.1. In order to test how robust the perturbative and combined factors were to the validity of perturbation theory, Gaussian power spectra with established validity were used. Surprisingly, scattering in 2D and 3D for Gaussian surfaces are similar away from specular without applying any factor, making the application of a factor inappropriate in this region. However, the spreading factor has some utility for the conversion of the specular peak from 2D to 3D in most cases (G4 breaks this trend). Lastly, in spite of the vast disagreement between perturbation theory and finite elements for G3 and G4, the perturbative factor remains conservative.

These factors provide a good first approximation for the comparison of two dimensional scattering models to three dimensional scattering. Though not ready for use as a component of a Navy standard model, they provide a new avenue to reduce the computation time of three dimensional computational models.

8.2 Future Work

As has been stated earlier in this thesis, the present work is meant to serve as a first step towards a method to compare 2D and 3D scattering. As such, there are a number of directions in which future work could proceed:

1. Alternate model ratios: The perturbative factor is simply the ratio of two approximate scattering models. This approach could be taken with any number of other approximate models. Specifically, this could be applied to the small-slope scattering model. This would be of much interest due to its large region of validity in comparison to first-order perturbation theory and to Kirchhoff theory. This small-slope factor could allow for a proper scaling of both the coherent and incoherent energy involved in scattering.

2. Out-of-plane scattering: Comparisons in this work were restricted to in-plane scattering ($\phi_s = 0$). It would be of interest to see how sound energy scatters into other directions and if that is predictable from 2D scattering models. Scattering out of plane for the VK parameters used in Section 7.1 is shown in Fig. 8.1.

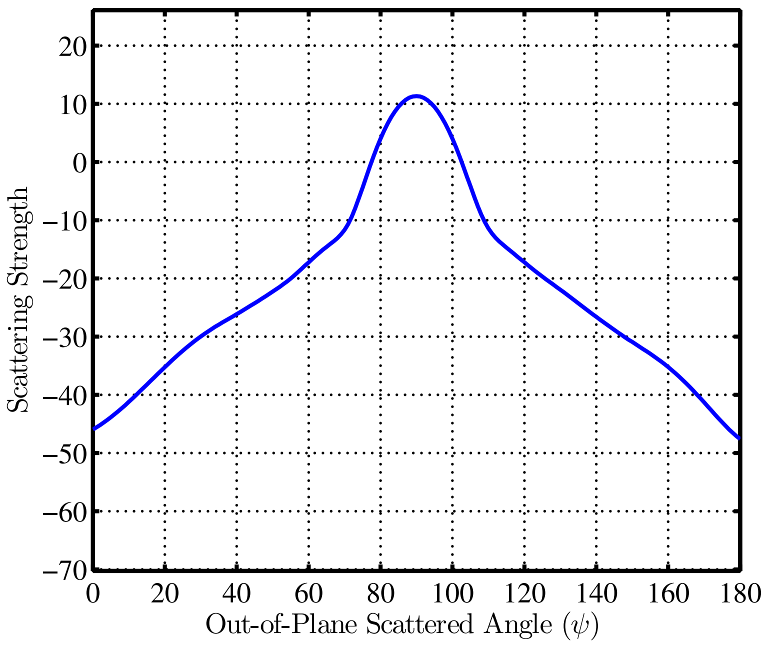

Figure 8.1: Out-of-plane scattering for VK parameters. Out-of-plane scattering angle refers to the angle from the positive y-axis going through the specular direction at 90 degrees and the negative y-axis at 180 degrees.

3. Penetrable bottoms: This work dealt only with a pressure-release bottom. The principles of this work could be easily applied to penetrable bottoms exhibiting a number of different behaviors including as a fluid medium, as an elastic medium, and as a poroelastic medium. This would, however, increase the difficulty of direct numerical simulation.

Appendices

Appendix A

Modeling Rough Surfaces in 3D Using COMSOL Multiphysics 4.3b

In order to model rough 2D surfaces in a 3D environment, there needs to be a way to describe surfaces explicitly. Unfortunately, this is not a simple task using the COMSOL Multiphysics environment. In previous versions used by Sumedh Joshi [1], there was a command called `geomsurf`, which allowed for a grid of z points given x and y positions that would create the surface. Unfortunately, there is no parallel to that command in the COMSOL 4.x scripting interface (LiveLink for MATLAB). Considerable effort was made by the author to determine a suitable replacement including the construction of multiple implementations that were not used in the final work. This appendix seeks to provide information regarding these methods.

A.1 STL Import

This method was used to generate the surfaces for work in this paper. It was chosen due to its simplicity and its similarity to `geomsurf`. Using this technique, the gridded z data is written to an STL file. This file type stores the surface as a collection of triangular facets with vertices specified by data.

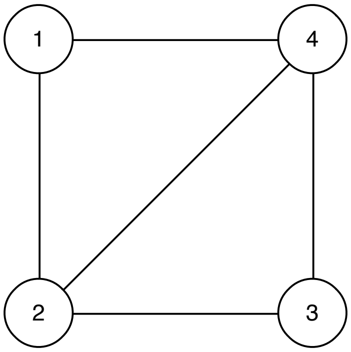

Figure A.1: Vertices of a single quadrilateral facet with imposed connectivity

In order to conform the grid of data (naturally a collection of quadrilaterals) into triangles, connectivity was added from vertex 2 to vertex 4 as shown in Fig. A.1 to divide each quadrilateral facet into two triangular facets.

The greatest advantage of this format is the ease of import into COMSOL. Rather than manually transfer data from a MATLAB session into COMSOL through various LiveLink interfaces, the STL file was simply written to disk and imported using an Import node within the Geometry sequence of COMSOL. This reduced latency of communication between the MATLAB and COMSOL sessions and simplified both the model tree and the command history. However, using the default settings for the Import node proved to be insufficient. Rather than allow for automatic merging of nearby facets, COMSOL was limited to only merging facets if the angle between them was 0, generally only occuring in the borders of the surface where it was forced to be flat.

A.2 Manually-Drawn Tesselation

This method is nearly identical to the method discussed in Sec. A.1 without the use of the Import command. Instead, for every triangular facet considered in the tesselation of the rough surface that would otherwise be written to the STL file, a triangle would be drawn. This would be accomplished through the creation of a work plane with the same normal vector as the facet itself where an appropriate triangle would be drawn. Despite the similarities of this technique to the STL import technique, it failed to be feasible for more than 100 triangles due to the complexity of the model tree and its toll on the command history. However, the results yielded identical results to the STL method for extremely coarse rough surface discretization.

A.3 Parametric Surface and Interpolation Table

The Parametric Surface geometry node allows for the definition of a surface in 3D via the evaluation of an expression parameterized by two parameters. In order to use this interface with discretized rough surfaces as used in this work, an interpolation function would have to be defined using x, y, and z data points from the surface, and then to evaluate this interpolation function over the appropriate x and y coordinates. Unfortunately, COMSOL internally represents the surface using a B-spline [18]. This ended up being problematic to how well the created surface matched the theoretical surface, especially in comparison to the `geomsurf` function.

A.4 Deformed Geometry

The use of the Deformed Geometry (DG) physics interface in COMSOL was attempted early on, the idea being to define the model geometry using a flat scattering surface and deforming parts of the surface in the $+z$ or $-z$ directions internally. This proved to be unsuccessful, but the author still believes that if this could be made to work, it would allow for a much simplified modeling process.

Bibliography

[1] S. M. Joshi, "Quantifying three dimensional effects in acoustic rough surface scattering", Master's thesis, The University of Texas at Austin (2011).

[2] P. J. Kaczkowski and E. I. Thorsos, "Application of the operator expansion method to scattering from one-dimensional moderately rough Dirichlet random surfaces", J. Acoust. Soc. Am. **96**, 957–972 (1994).

[3] D. R. Jackson and M. Richardson, *High-frequency seafloor acoustics* (Springer, New York) (2007).

[4] J. W. S. Rayleigh, *The Theory of Sound*, 2d ed. rev. and enl edition (Dover publications, New York) (1945).

[5] U. Fano, "The theory of anomalous diffraction gratings and of quasi-stationary waves on metallic surfaces (Sommerfeld's waves)", J. Opt. Soc. Am. **31**, 213–222 (1941).

[6] S. O. Rice, "Reflection of electromagnetic waves from slightly rough surfaces", Commun. Pure Appl. Math. **4**, 351–378 (1951).

[7] M. Isakson, N. Chotiros, R. Yarbrough, and J. Piper, "Quantifying the effects of roughness scattering on reflection loss measurements", J. Acoust. Soc. Am. **132**, 3687–3697 (2012).

[8] M. J. Isakson and N. P. Chotiros, "Finite element modeling of reverberation and transmission loss in shallow water waveguides with rough boundaries", J. Acoust. Soc. Am. **129**, 1273–1279 (2011).

[9] K. F. Warnick and W. C. Chew, "Numerical simulation methods for rough surface scattering", Waves in Random Media **11**, R1–R30 (2001).

[10] T. von Karman, "The fundamentals of the statistical theory of turbulence", J. Aeronaut. Sci. **4**, 131–138 (1937).

[11] E. Thorsos, "The validity of the Kirchhoff approximation for rough surface scattering using a Gaussian roughness spectrum", J. Acoust. Soc. Am. **83**, 78–92 (1988).

[12] J. A. Ogilvy, *Theory of wave scattering from random rough surfaces* (A. Hilger, Bristol, England) (1991).

[13] M. Isakson, R. Yarbrough, and N. Chotiros, "A finite element model for seafloor roughness scattering", in *Proceedings of the International Symposium on Underwater Reverberation and Clutter* (2008).

[14] T. M. Elfouhaily, C.-A. Guérin, *et al.*, "A critical survey of approximate scattering wave theories from random rough surfaces", Waves in Random Media **14**, R1–R40 (2004).

[15] M. Abramowitz and I. Stegun, *Handbook of mathematical functions with formulas, graphs, and mathematical tables,* (U.S. Govt. Print. Off., Washington) (1964).

[16] D. T. Blackstock, *Fundamentals of Physical Acoustics* (John Wiley & Sons, New York) (2000).

[17] E. Becker, G. Carey, and J. Oden, *Finite Elements: An Introduction, Volume I* (Prentice-Hall, Englewood Cliffs, N.J) (1981).

[18] COMSOL, Inc., *COMSOL Multiphysics 4.3b Documentation*.

[19] L. Tsang, C. H. Chan, and K. Pak, "Backscattering enhancement of a two-dimensional random rough surface (three-dimensional scattering) based on monte carlo simulations", J. Opt. Soc. Am. **11**, 711–715 (1994).

[20] M. Zampolli, A. Tesei, F. B. Jensen, N. Malm, and J. B. Blottman III, "A computationally efficient finite element model with perfectly matched layers applied to scattering from axially symmetric objects", J. Acoust. Soc. Am. **122**, 1472–1485 (2007).

[21] B. Tran, S. Joshi, and M. Isakson, "Applicability of two-dimensional boundary scattering models as a proxy for three-dimensional models", in *Proceedings of Meetings on Acoustics*, volume 19, 70–79 (2013).

[22] D. Jackson, R. Odom, M. Boyd, and A. Ivakin, "A geoacoustic bottom interaction model (GABIM)", IEEE J. Ocean. Eng. **35**, 603–617 (2010).

Vita

Bryant Minh Tran was born in Austin, Texas. After graduating from the Liberal Arts and Science Academy at Lyndon Baines Johnson High school in 2006, he studied Electrical and Computer Engineering at the University of Texas at Austin. During the summers of 2006-2008, he worked as an intern in the Systems and Technology Group at IBM. After graduating with a Bachelor of Science in 2010, he entered graduate school at The University of Texas studying Acoustics, and started work at the Applied Research Laboratories of the University of Texas at Austin.

Permanent address: bmtran@utexas.edu

This thesis was typeset with LaTeX[†] by the author.

[†] LaTeX is a document preparation system developed by Leslie Lamport as a special version of Donald Knuth's TeX Program.